**Journal of Oceanology and Limnology**
**Vol. 44, No. 5, pp. 1833-1845, 2026**
**https://doi.org/10.1007/s00343-026-6004-9**

Research Paper

# Water-leaving reflectance correction and transparency estimation based on RAW-format smartphone photos*

Min GAO[1, 2, 3, 4], Junsheng LI[2, 4, 5, **], Shenglei WANG[2, 4], Fangfang ZHANG[2, 4], Huaxin YAO[2, 4, 6], Xuezhu JIANG[2, 4, 6]

[1] *Inspection and Support Center, Department of Natural Resources of Inner Mongolia Autonomous Region, Hohhot 010010, China*

[2] *Key Laboratory of Digital Earth Science, Aerospace Information Research Institute, Chinese Academy of Sciences, Beijing 100094, China*

[3] *School of Earth Science and Resources, China University of Geoscience, Beijing 100083, China*

[4] *International Research Center of Big Data for Sustainable Development Goals, Beijing 100094, China*

[5] *School of Electronic, Electrical and Communication Engineering, University of Chinese Academy of Sciences, Beijing 100049, China*

[6] *College of Resources and Environment, University of Chinese Academy of Sciences, Beijing 100049, China*

Received Jan. 4, 2026; accepted in principle Mar. 19, 2026; accepted for publication Apr. 13, 2026

© Chinese Society for Oceanology and Limnology, Science Press and Springer-Verlag GmbH Germany, part of Springer Nature 2026

**Abstract** In the field of water color remote sensing and environmental monitoring, smartphone-acquired water imagery has emerged as a powerful tool for crowdsourced surveillance. However, the widely used Joint Photographic Experts Group (JPEG) format presents significant challenges for accurate water-leaving reflectance (remote sensing reflectance) correction and water quality monitoring. To address these issues, this study puts forward a high-precision method for water-leaving reflectance calibration and transparency inversion using RAW-format photos captured by smartphones. The digital number (DN) values in RAW-format photos exhibit a linear relationship with reflectance, with the regression line closely passing through the origin. This allows for the conversion of DN values of water and sky photos into reflectance using a single gray reference card with known reflectance, enabling more precise calculation of water-leaving reflectance. Validation with data from 267 sampling points across 15 study regions in China showed an average $R^2$ of 0.93 in the blue, green, and red spectral bands. When the calibrated reflectance was applied to transparency inversion, the modified QAA-RGB semi-analytical model outperformed the semi-empirical model, achieving an $R^2$ of 0.78. These results provide a solid technical foundation for using smartphones to achieve high-precision, crowdsourced water quality monitoring in the context of water color remote sensing. This study focuses on the linear response characteristic of RAW format data. Through large-scale, cross-regional validation, smartphone-based water quality monitoring is extended from reflectance correction to parameter inversion. Consequently, threefold breakthroughs are achieved in methodological simplification, validation robustness, and application scope.

**Keyword**: smartphone; crowdsourced surveillance; RAW; Joint Photographic Experts Group (JPEG); water-leaving reflectance; transparency

## 1 INTRODUCTION

Water quality monitoring is a critical component of water environment management and protection. Traditional monitoring methods primarily rely on field sampling and laboratory analysis, which, while offering high accuracy, are time-consuming, labor-

* Supported by the National Natural Science Foundation of China (No. 42271363), the Scientific and Disruptive Technology Research Fund Project of Aerospace Information Research Institute, Chinese Academy of Sciences (No. 2025-AIRCAS-SDTP-16), and the Future Star Program of the Aerospace Information Research Institute

** Corresponding author: lijs@radi.ac.cn

intensive, and limited in spatial coverage and temporal resolution (He et al., 2024; Hu et al., 2025; Jiang et al., 2025). These limitations make it challenging to meet the demands of monitoring dynamic changes in complex aquatic environments (Zhang et al., 2021a). Online monitoring technologies based on shore-based or in-water stations have significantly increased the temporal frequency of measurements, but their high construction and maintenance costs, along with limited spatial coverage, remain major constraints (Zhang et al., 2021b). Satellite remote sensing, with its broad coverage, rapid data acquisition, and low cost, has become an essential tool for large-scale water quality monitoring (Odermatt et al., 2018; Wang et al., 2018, 2020; Zeng et al., 2023; Cao et al., 2024; Song et al., 2025). However, remote sensing imagery is often subject to limitations such as cloud cover, imaging cycles, and insufficient spatial resolution (Yin et al., 2023; Feng and Wang, 2024; Wang et al., 2024).

In recent years, smartphones have emerged as a promising tool for water quality monitoring due to their portability, wide accessibility, and increasingly advanced imaging capabilities (Duan et al., 2019; Li et al., 2022; Huang et al., 2024). A critical challenge in using smartphone-captured water surface photos for high-precision, quantitative water quality monitoring lies in the calibration of water-leaving reflectance (technically termed remote sensing reflectance, $R_{rs}$), which is essential to eliminate interference from ambient light and sky-glare reflections on the water surface (Gao et al., 2020, 2022). Although some exploratory studies have been conducted, these typically involve capturing reference card, water surface, and sky photos using the smartphone camera's automatic exposure mode, followed by normalization based on exposure parameters, and then applying the "above-water method" for reflectance calibration of the water photos (Leeuw and Boss, 2018; Mahama and Salama, 2024a, b).

However, these studies do not account for the nonlinear response mechanism of the digital numbers (DN) in Joint Photographic Experts Group (JPEG) photos to incident light intensity. Specifically, cameras employ gamma correction to mimic the nonlinear response of the human eye to varying light intensities (bright areas are compressed, dark areas are expanded), leading to significant errors when normalization is applied to photos captured with different exposure settings (Malthus et al., 2020; Li et al., 2022).

A study (Burggraaff et al., 2019) proposed and a follow-up study (Burggraaff et al., 2022) demonstrated that using RAW format photos for remote sensing reflectance calibration could improve the accuracy. However, this approach has only been tested on a few water bodies, and has not been evaluated for its application in further water quality monitoring.

This study addresses these issues by investigating the advantages of RAW format photos over JPEG format photos for remote sensing reflectance correction. We then use a more diverse set of water body samples than previous studies to validate the proposed methods. Finally, we refine these methods for both reflectance correction and inversion of typical water quality parameters based on smartphone RAW format photos. We acquire RAW-format water photos and corresponding field-measured spectral and water quality data from a wide range of water bodies with varying characteristics. This will enable the evaluation of the applicability of the RAW-format-based remote sensing reflectance calibration method and further assess its effectiveness in water quality monitoring. The water quality parameter to be retrieved in this study is transparency, which is a key indicator of water clarity and is closely related to the concentration of suspended particulate matter, algae, and dissolved organic matter. This study will contribute to enhancing the effectiveness of smartphone-based water quality monitoring, providing a robust tool for crowdsourced water quality monitoring.

## 2 DATA

### 2.1 Study area

In this study, water surface experiments were conducted at 267 sampling sites across 15 lake, reservoir, and river study areas in China from 2017 to 2023. These study areas, located in various regions including North China, East China, Central China, Southwest China, and Northwest China, encompass water bodies with varying levels of turbidity and nutrient status. The distribution of the study areas is shown in Fig.1a.

### 2.2 Water surface experiment data acquisition

At each sampling site, reference card, water surface, and sky photos were captured, alongside in situ above-water reflectance collection and transparency measurements.

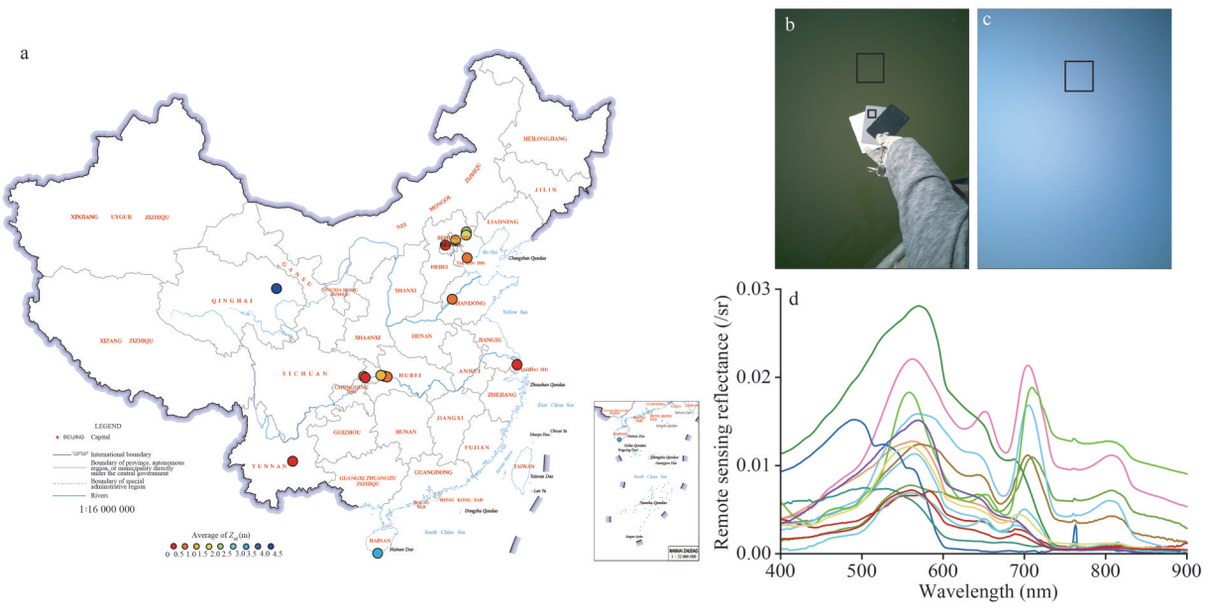


**Fig.1 Distribution of study areas, photo capture, and spectral measurement results**

a. distribution of study areas and mean transparency values; b. example photos of water body from the study areas (black boxes indicate the cropped water surface and reference card areas); c. example photos of the sky from the study areas (black boxes indicate the cropped sky regions); d. typical field-measured remote sensing reflectance spectra for each study area. Map review No. GS(2019)1686.

### 2.2.1 Raw-format photos acquisition

This study utilized a Huawei Mate 30 smartphone and a Canon EOS 50D camera to capture RAW-format photos. To calculate the remote sensing reflectance, photos of three objects were taken: the water surface, a reference card, and the sky. The reference card is used to convert the photo DN values into reflectance, while the sky photos are used to correct the skylight reflected by water surface. The reference card used in this study is a gray card commonly employed for white balance in photography, with a reflectance of approximately 18%. Using this gray card offers two advantages. Firstly, its reflectance is close to that of water bodies, so when photographed alongside water, their brightness levels are similar, preventing overexposure or underexposure of specific targets. Secondly, this photographic gray card is both convenient to purchase and inexpensive, making it suitable for subsequent promotion in crowdsourced monitoring efforts.

The reference card and water body are photographed simultaneously which helps minimize the impact of different exposure settings. It should be noted that when photographing the reference card and water body, the reference card should be extended as far away from the operator as possible. Doing so offers two advantages. Firstly, it helps mitigate the effects of reflections from the operator and the surrounding shoreline or the hull of the vessel. Secondly, the reference card occupies a relatively small proportion of the image, ensuring that the central part of the reference card and the adjacent water body are observed from similar angles. This reduces discrepancies in lighting conditions between the water and the reference card caused by differences in observation angles. Additionally, when photographing the reference card and water body, it is important to avoid allowing shadows from surrounding objects to affect either the reference card or adjacent water area.

Unlike the reference card, the sky could not be photographed simultaneously with the water and had to be captured separately. The challenges of using a digital camera to capture remote sensing radiance are similar to those encountered when using conventional spectrometers; both require minimizing the influence of sun glint, boat hulls, or shorelines. Therefore, to obtain water-leaving radiance using the camera, the “above-water method” from ocean optics guidelines was applied (Mueller and Fargion, 2002). When photographing the water surface and reference card, the azimuth angle of observation relative to the sun was approximately 135°, and the zenith angle was approximately 40° outward from vertical. For the sky photos, the azimuth angle was also about 135° relative to the sun, with the zenith angle directed

approximately 40° outward from vertical. During the photo capture process, the aperture was fixed, and the shutter speed was adjusted to vary the exposure.

The photographs of the water body, reference card, and sky light at the typical sampling sites captured in this study are shown in Fig.1b & c. It should be noted that the displayed photos have been converted to JPEG format.

2.2.2 Remote sensing reflectance collection

Based on the "above-water method" (Mueller and Fargion, 2002), radiance measurements from the portable field spectroradiometer were conducted at each site to capture the radiance of the reference panel ($L_p$), total water surface radiance ($L_u$), and downwelling sky radiance ($L_{sky}$). The spectroradiometer used in this study is the ASD Field Spec 4, with a wavelength range of 400–2 500 nm. $R_{rs}$ was then calculated using the spectral data according to Eq.1 (Lee et al., 2016):

$$R_{rs} = \frac{L_u - r_{sky} \times L_{sky}}{L_p \times \pi / R_p} - \Delta, \quad (1)$$

where, $r_{sky}$ represents the reflectance of sky radiance at the air-water interface, and can be calculated by the Fresnel formula. $R_p$ is the reflectance of the reference panel, which has been calibrated in the laboratory. $\Delta$ is a bias, and can be estimated by assuming $R_{rs}$ in near infrared or short-wave infrared is 0 (Lee et al., 2016).

After dark current correction, the spectroradiometer captured radiance ($L$) can be expressed as gain×DN. The gain factor cancels out in the numerator and denominator in Eq.1, and Eq.1 can be replaced by the following Eq.2:

$$R_{rs} = \frac{DN_u - r_{sky} \times DN_{sky}}{DN_p \times \pi / R_p} - \Delta. \quad (2)$$

Therefore, the spectroradiometer itself does not require radiometric calibration to obtain the actual gain factor, whereas the reflectance of the reference panel still needs calibration.

The representative remote sensing reflectance results calculated for the 15 study areas are shown in Fig.1d. As seen in the figure, the spectral characteristics of the water bodies across these study areas vary significantly.

2.2.3 Transparency measurement

At each sampling site, water transparency ($Z_{sd}$) was measured using the conventional Secchi disk method. In this approach, the Secchi disk was gradually lowered into the water, and the depth at which it disappeared from the observer's line of sight was recorded as the water transparency.

The average transparency for all sites in each study area was calculated, as represented by the differently colored dots in Fig.1a. From the figure, it is evident that there is a significant variation in water transparency across the study areas, ranging from very clear waters with transparency greater than 4.0 m (e.g., Qinghai Lake) to highly turbid waters with transparency less than 0.5 m (e.g., Taihu Lake).

# 3 METHOD

## 3.1 Comparative analysis of optical response between RAW and JPEG format photos

To evaluate the advantages of RAW format photos over JPEG format photos in terms of optical response, we designed the following comparative analysis experiment. Prior to the optical response experiment, a brief introduction to the processing steps of RAW format photos is necessary.

3.1.1 RAW photo processing workflow

Figure 2 illustrates the main process from photo capture to generation. To intuitively illustrate the process by which a camera produces RAW and JPEG images, a pure yellow target object was used. Due to differences in the output files generated from the target object during photo capture, the target may appear differently. To avoid confusion with the output photos, no specific color is assigned to the target object. In the camera, the CMOS sensor is coated with a Bayer filter (blue, green, red) (Lukac and Plataniotis, 2006), and the resulting RAW photo is a mixed-band grayscale photo. Due to the varying light transmission of the Bayer filter, the yellow target produces a RAW grayscale photo with uneven brightness, resulting in a mosaic pattern. Specifically, from the mosaiced image, the pixel values corresponding to the R pixels of the Bayer filter were first selected. The pixel values for the G and B pixels were then obtained by interpolating from the neighboring R pixel values using a spatially uniform interpolation method. In this way, images for the R, G, and B bands were each reconstructed through separate interpolation. The interpolated three-band photo can then be merged into a TIFF format file for subsequent above-water reflectance calibration and water quality parameter

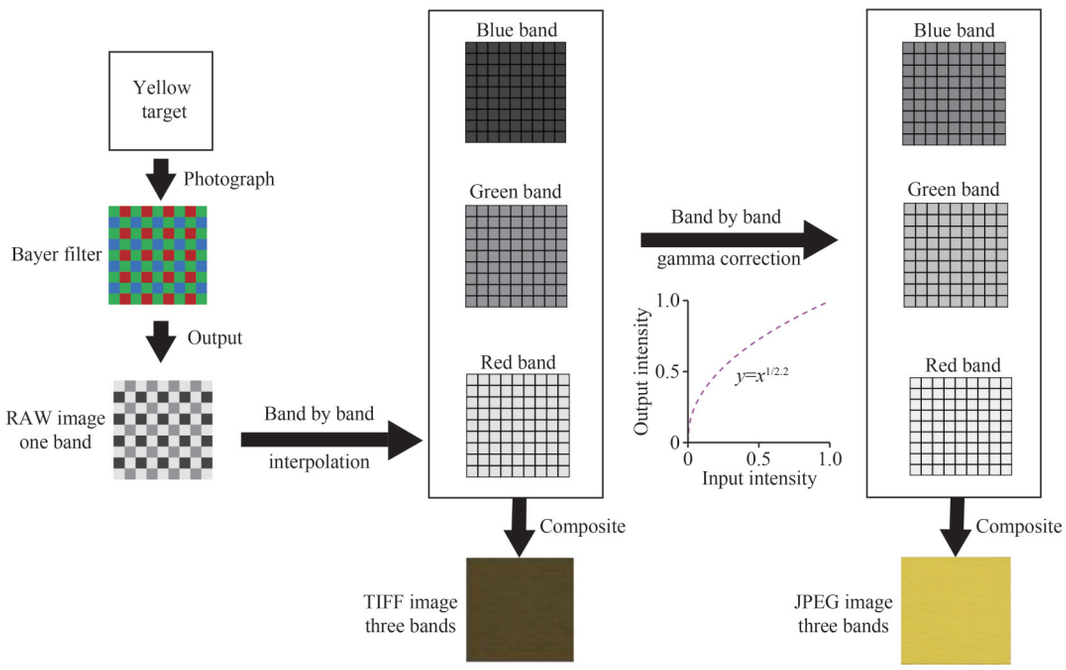


**Fig.2 The primary process of photo generation from the target object captured by the digital camera**

inversion. The JPEG photo is generated by simulating the human eye's nonlinear gamma response to light, which stretches low-end signals and compresses high-end signals. After gamma correction, the three-band photo is synthesized and compressed into JPEG format. The JPEG images used in this study were all generated using Dcraw (https://github.com/ncruces/dcraw/releases/download/v9.28.4-win) from the RAW-format photos captured by the camera.

3.1.2 Design of optical response experiment

This study designed two optical response experiments. In the first experiment, the exposure time was varied across 12 sets while maintaining a fixed aperture and ISO on a smartphone, ensuring the photos were not overexposed. Both RAW and JPEG formats were used to capture the same target object. In the second experiment, both RAW and JPEG formats were used to capture a single photo of five reference panels with different reflectance values, as shown in Fig.3b. Figure 3a presents the spectral response functions of the blue, green, and red bands of the camera (Prasad et al., 2013), along with the reflectance curves of the five reference panels. The reflectance curves of the reference panels were converted into equivalent reflectance for each spectral band of the Canon EOS 50D camera using the spectral response curve of the

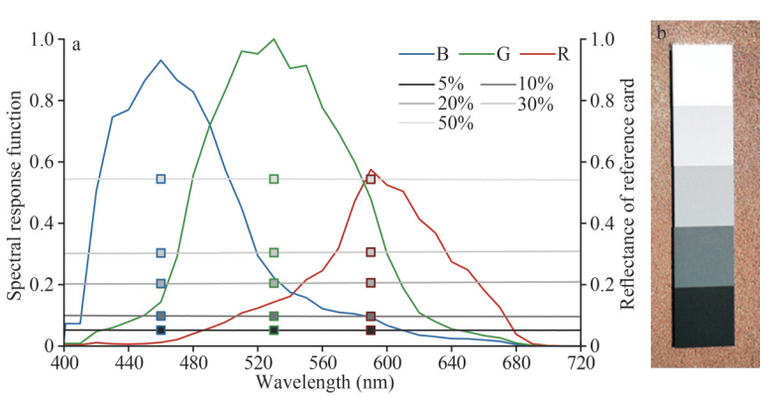


**Fig.3 Spectral response functions for the blue, green, and red bands of the digital camera, reflectance curves of five reference panels, and the equivalent band reflectance results derived using the spectral response functions (small rectangles) (a); photograph of the five reference panels with varying reflectance values (b)**

Canon EOS 50D camera (Gao et al., 2020), with the resulting values displayed as rectangles in Fig.3a.

### 3.2 Remote sensing reflectance calibration method based on RAW format photos

After obtaining the water surface photos using the RAW photo acquisition method outlined in Section 2.2, the next step in calculating transparency from the photos is to first compute the remote sensing reflectance of the water surface.

#### 3.2.1 Photo cropping and extraction of DN value median

First, the Dcraw program is used to read all RAW format photos and convert them into grayscale TIFF photos. Next, the TIFF files of the reference card, water surface, and sky are opened. The reference card and water surface are cropped separately, ensuring that areas affected by solar glint, shadows, and floating debris are avoided during the cropping of the water surface. Then, the TIFF file of the sky is opened and cropped accordingly. Finally, the cropped reference card, water surface, and sky photos are properly named to facilitate subsequent batch processing. Each cropped photo corresponding to the reference card, water surface, and sky for each site is then batch-read, and the median DN values of the photos are calculated and saved.

#### 3.2.2 Calculation of remote sensing reflectance

Based on the optical response of the RAW photos, a linear model is fitted between the reflectance of the reference card ($R_p$) and the corresponding median DN value ($DN_p$) of the cropped photo, as follows:

$$R_p = \text{scale} \times DN_p. \tag{3}$$

Using the $DN_p$ values of the reference card photos captured at each site and their corresponding calibrated reflectance values ($R_p$), the scale coefficient is determined. This coefficient represents the relationship between the DN values and their reflectance of the reference card and the water surface photos at that site. Using this relationship, the reflectance of the water surface ($R_w$) can be calculated from its DN value ($DN_w$):

$$R_w = \text{scale} \times DN_w. \tag{4}$$

It is important to note that the DN-reflectance relationship established with the reference card applies only to the reference card and water surface photos captured under identical exposure conditions. When capturing sky photos, however, the shutter speed is typically shorter for sky photos than for water surface photos, as the sky is generally brighter. To apply the DN-reflectance relationship derived from the reference card photo, a shutter time correction must be applied to the sky photos.

For RAW format photos, when the aperture and ISO are fixed while the shutter time is varied, the DN value of the same object is approximately proportional to the shutter time ($T$). Therefore, the shutter time correction for the sky photo ($T_s$) can be applied using the shutter times of the reference card photo ($T_p$) and the sky photo, resulting in the corrected DN value for the sky photo ($DN_{sc}$). The correction formula is as follows:

$$DN_{sc} = DN_s / T_s \times T_p. \tag{5}$$

By substituting the shutter-corrected sky DN value ($DN_{sc}$) into the reflectance calibration formula based on the reference card photo, the sky reflectance ($R_s$) can be calculated.

$$R_s = \text{scale} \times DN_{sc}. \tag{6}$$

Since Eq.4 and Eq.6 both represent reflectance, while Eq.2 represents DN values. To establish a connection among the three formulas, the original Eq.2 was transformed as follows (ignoring the -Δ):

$$\begin{aligned} R_{rs} &= \frac{DN_u}{DN_p \times \pi / R_p} - r_{sky} \times \frac{DN_{sky}}{DN_p \times \pi / R_p} \\ &= (R_w - r_{sky} \times R_s)/\pi, \end{aligned} \tag{7}$$

$$R_w = \frac{DN_u}{DN_p / R_p}, \tag{8}$$

$$R_s = \frac{DN_{sky}}{DN_p / R_p}. \tag{9}$$

#### 3.2.3 Accuracy assessment

Using the spectral response functions of the camera's blue, green, and red bands, the remote sensing reflectance spectra measured at each site, as described in Section 2.2.2, can be equivalently mapped to the camera's blue, green, and red bands. Strictly speaking, the calculation should be performed using underlying radiances (Burggraaff, 2020). However, given that the practical impact is relatively small and underlying radiances are not readily accessible, the method is instead applied to reflectance (Wang et al., 2020; Luo et al., 2023). These band-equivalent remote sensing reflectance values serve as the reference data for evaluating the accuracy of the remote sensing reflectance calibration of the RAW format photos. The accuracy

assessment is performed using metrics such as root mean square error (RMSE), mean relative error (MRE), ratio and coefficient of determination ($R^2$). The formulas for calculating RMSE, MRE, the ratio and $R^2$ are as follows:

$$\mathrm{RMSE}=\sqrt{\sum_{i=1}^{N}(Y_i-X_i)^2/N}, \tag{10}$$

$$\mathrm{MRE}=\sum_{i=1}^{N}\left(\frac{|Y_i-X_i|}{X_i}\right)/N, \tag{11}$$

$$\mathrm{ratio}=\sum_{i=1}^{N}\left(\frac{Y_i}{X_i}\right)/N, \tag{12}$$

$$R^2=1-\frac{\sum_{i=1}^{N}(X_i-Y_i)^2}{\sum_{i=1}^{N}(X_i-\overline{X})^2}, \tag{13}$$

where, $N$ represents the number of sampling points; $X_i$, $\overline{X}$, and $Y_i$ correspond to the reference data value at each sampling point, the mean of the reference data values, and the digital photo estimated value, respectively.

The Pearson correlation coefficient between the two datasets was calculated. A coefficient value closer to 1 indicates a higher similarity in spectral shape between the two datasets, whereas a value farther from 1 indicates a lower similarity.

### 3.3 Transparency inversion method based on visible bands remote sensing reflectance

This study primarily compares two models for retrieving water transparency: the empirical model and the semi-analytical model. To make full use of water samples from different types, two-thirds of the data from each study area were selected to form the training dataset, and the remaining one-third were used as the validation dataset. This stratified random sampling strategy can improve the model generalizability compared to methods like random sampling (Ramezan et al., 2019). The empirical model establishes a statistical relationship between the remote sensing reflectance retrieved from digital photos at 2/3 of the sampling points and the corresponding in-situ measured transparency. The remaining 1/3 of the sampling points are used for accuracy assessment. The spectral indices employed in the empirical model include the red band reflectance ($R_{rs}$(R)), the difference between the blue and green band reflectance ($R_{rs}$(B)–$R_{rs}$(G)), and the ratio of the red band reflectance to the mean of the blue and green band reflectance ($R_{rs}$(R)/(($R_{rs}$(G)+$R_{rs}$(B))/2)) (Yin et al., 2021a, b). The semi-analytical model is based on a transparency retrieval algorithm derived from the quasi-analytical algorithm (QAA) (Lee et al., 2015). Given that digital photos only provide blue (B), green (G), and red (R) bands, the transparency retrieval is conducted using the QAA-RGB algorithm (Pitarch and Vanhellemont, 2021). The core principles and steps of the QAA-RGB algorithm are detailed in Supplementary Table S1. Since the QAA-RGB algorithm does not directly account for the spectral characteristics of digital photos, it was necessary to adapt the algorithm. This enhancement involved fitting polynomial coefficients suitable for digital photos using the IOCCG dataset (IOCCG, 2006), as described in Supplementary Figs.S1–S3 & Tables S2–S4.

Finally, the accuracy of the empirical and semi-analytical models was compared to identify the model best suited for retrieving transparency from digital photos.

## 4 RESULT

### 4.1 Analysis of the optical response of RAW-format photos

From Fig.4, it can be observed that the DN values of RAW-format photos exhibit a linear relationship with exposure time, with a linear regression Pearson correlation coefficient ($r$) of 0.99. This indicates that DN values can be normalized and calibrated according to the exposure times when capturing different targets. In contrast, the DN values of JPEG-format photos follow a nonlinear relationship with exposure time, best described by a gamma function with $r$ of 0.99. Consequently, JPEG photos are less suitable for normalization based on exposure time, because at least three exposure times are required to capture the same target object separately in order to fit the nonlinear relationship between the DN values and the exposure times.

Figure 5 illustrates that for RAW-format photos, the DNs of the five reference cards have a linear relationship with their reflectance values, with the regression line passing near or through the origin ($R^2$=0.99). Thus, it is possible to convert DN values to reflectance using only a single reference card with known reflectance. For JPEG photos, the relationship between DN values and reflectance is nonlinear, with a power function regression

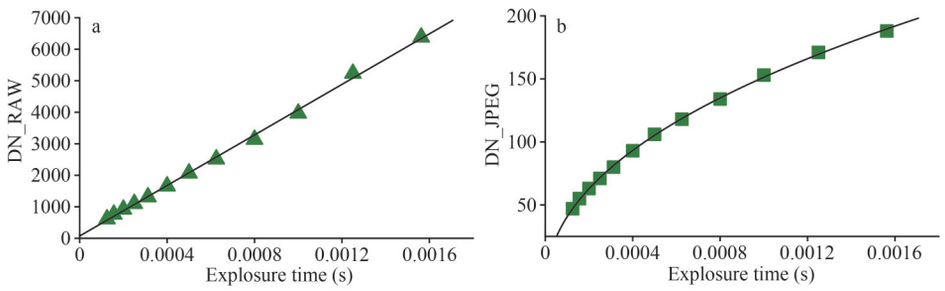


**Fig.4 Relationship between DN values of the green band for the reference card and exposure time**

a. RAW-format photos; b. JPEG-format photos.

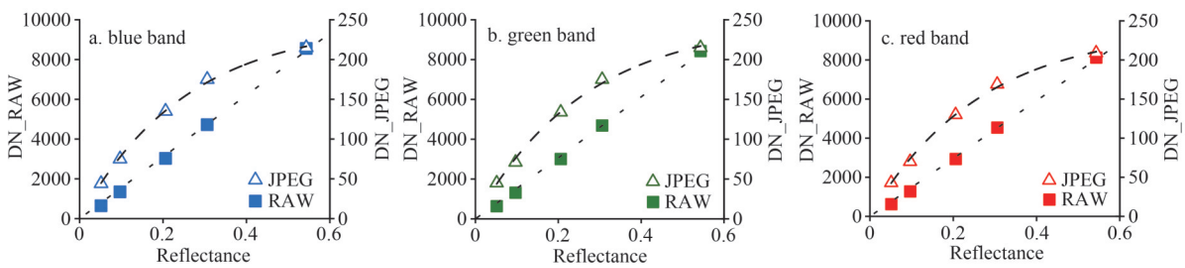


**Fig.5 Relationship between the DNs of five reflectance reference panels and their reflectance**

achieving an $R^2$ of 0.96. This necessitates at least three reference cards with varying reflectance to establish the DN-to-reflectance relationship.

### 4.2 Accuracy evaluation of remote sensing reflectance correction for RAW-format water surface photos

Using the method for remote sensing reflectance correction described in Section 3.2, the DN values of the reference cards, water bodies, and sky from 267 sampling points across 15 study areas were converted into remote sensing reflectance for RAW-format photos. The scatter plots comparing reflectance derived from RAW-format photos ($R_{rs_m}$) and spectrometer-measured equivalent remote sensing reflectance ($R_{rs_p}$) areshown in Fig.6.

In Fig.6, the scatter plots for the blue, green, and red bands align closely with the 1:1 line, with $R^2$ values ranging from 0.89 to 0.98, Ratios from 0.87 to 0.91, and MRE between 31.2% and 43.1%. The slightly high MRE is likely due to certain points with low remote sensing reflectance, which disproportionately affect the overall error.

The absolute accuracy of the remote sensing reflectance values for the blue, green, and red bands has been quantitatively evaluated. To further assess the accuracy of the spectral shapes, the reflectance spectra for all 267 sampling points derived from the three bands were compared to their spectrometer-measured equivalents. The $r$ between the two sets of spectra revealed that 80% of the sampling points had $r$ values exceeding 0.8.

In summary, the accuracy of the remote sensing

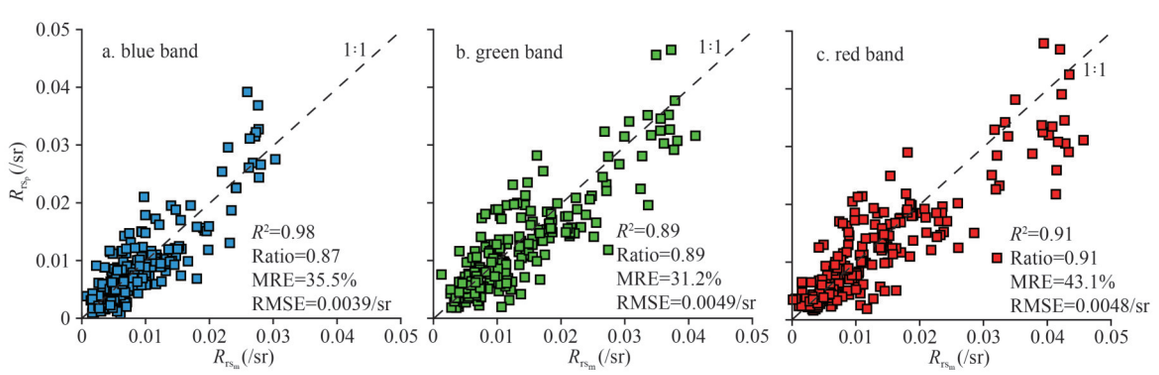


**Fig.6 Scatterplots comparing remote sensing reflectance derived from corrected RAW-format water surface photos ($R_{rs_p}$) and in situ equivalent measurements ($R_{rs_m}$) across 267 sampling points in 15 study areas**

reflectance correction is relatively high, supporting its further application in retrieving water quality parameters.

### 4.3 Transparency retrieval result based on remote sensing reflectance

The remote sensing reflectance derived from the photos for 267 sampling points was combined with concurrent transparency measurements to construct and evaluate a semi-empirical transparency retrieval model. First, the remote sensing reflectance derived from 2/3 of the raw format photos is used to compute three spectral indices, which are then applied to develop an inversion model by training it with the measured transparency data from the same 2/3 of the sampling points. The trained semi-empirical model was then validated on the remaining 1/3 of the data, with in-situ transparency measurements serving as ground truth. The semi-empirical model and its accuracy metrics are summarized in Table 1.

As shown in Table 1, the semi-empirical model based on the spectral index $R_{rs}(R)/((R_{rs}(G)+R_{rs}(B))/2)$ achieved the highest accuracy among the tested models.

Additionally, the QAA-RGB-based semi-analytical model was optimized using 2/3 of the experimental data, with detailed optimization results provided in Supplementary Fig.S3. Validation of the optimized model on the remaining 1/3 of the data yielded accuracy metrics of $R^2$=0.78, RMSE=0.6 m, MRE= 45.4%, and ratio=0.85, as shown in Supplementary Fig.S4. The transparency retrieval accuracy of the semi-analytical model was notably higher than that of the semi-empirical model. These results suggest that the semi-analytical model better captures the physical relationship between remote sensing reflectance spectra and transparency, offering superior generalizability and accuracy.

## 5 DISCUSSION

### 5.1 Remote sensing reflectance correction for different scenes

The foundational premise of this study is the superior optical response of RAW format photos compared to the JPEG format. Experimental results robustly confirm this viewpoint. As illustrated in Fig.4, a linear relationship exists between the DN values of RAW format photos and the exposure time, whereas the JPEG format exhibits a non-linear relationship. This fundamental discrepancy necessitates the use of multiple exposure times or multiple reflectance reference cards to fit a complex non-linear relationship when using JPEG photos, significantly increasing the complexity and uncertainty of field operations. In contrast, the linear response of the RAW format enables precise remote sensing reflectance correction using only a single gray reference card (such as the 18% reflectance gray card used in this study), offering considerable convenience for public participation in crowdsourced water quality monitoring.

Similarly, Fig.5 clearly demonstrates the linear relationship between the DN values of the RAW format and the target reflectance, with the regression line passing near the origin. This characteristic is not only the basis for its high-precision calibration but also simplifies the data processing workflow. Although JPEG is feasible for qualitative monitoring, the non-linear response of JPEG limits its application in high-precision quantitative remote sensing.

Regarding whether to perform remote sensing reflectance correction, we believe that both technical strategies have their own applicable scenarios and should be flexibly selected according to actual conditions. Reflectance correction using a reference card can effectively eliminate interference from variations in incident illumination and specular reflection of sky light on the water surface, yielding reflectance data that more closely represent the true optical properties of water. This theoretically improves the accuracy and stability of water quality parameter inversion models, making it suitable for monitoring tasks that require high quantification. On the other hand, direct water quality monitoring based on raw DN values is also feasible. Existing

**Table 1 Accuracy evaluation of transparency retrieval using three semi-empirical models based on corrected remote sensing reflectance**

| Spectral index ($x$) | Modeling | | Validation | | | |
|---|---|---|---|---|---|---|
| | Model | $R^2$ | RMSE (m) | MRE (%) | Ratio | $R^2$ |
| $R_{rs}(R)$ | $Z_{sd}=0.026x^{-0.70}$ | 0.60 | 1.2 | 40.96 | 0.26 | 0.55 |
| $R_{rs}(G)–R_{rs}(B)$ | $Z_{sd}=2.07e^{-215.76x}$ | 0.61 | 1.0 | 54.02 | 0.36 | 0.71 |
| $R_{rs}(R)/((R_{rs}(G)+R_{rs}(B))/2)$ | $Z_{sd}=1.06x^{-2.02}$ | 0.58 | 0.7 | 58.56 | 0.61 | 0.74 |

studies (Li et al., 2022, 2024) have shown that DN values can be used for water quality parameter inversion even without reflectance correction, although the results are more susceptible to environmental illumination and thus have higher uncertainty. Considering both operational convenience and inversion accuracy, this study recommends selecting the appropriate strategy based on field conditions: when a reference card is available, prioritize reflectance correction to ensure inversion accuracy; when a reference card cannot be used, construct water quality monitoring models directly from raw DN values.

### 5.2 Comparison with literature and methodological improvements

This study does not represent the first attempt to employ smartphones for water quality monitoring. Rather, it constitutes a significant evolution and a substantive breakthrough built upon the foundation of prior research. The methodological improvements and comparative advantages are detailed below.

(1) Advancement beyond JPEG-based methods

When compared with Gao et al. (2020) and Gao et al. (2022), the pivotal advancement of this study lies in the explicit recognition and utilization of the linear response characteristic inherent to RAW format data. The earlier studies primarily relied on JPEG format imagery or employed multiple reference cards to compensate for its inherent non-linear response, resulting in comparatively complex operational procedures. This study conclusively demonstrates that by leveraging the fundamental properties of RAW format photos, high-precision remote sensing reflectance correction can be achieved using only a single reference card. This breakthrough dramatically simplifies the operational workflow and significantly lowers the technical barrier, making sophisticated monitoring feasible for crowdsourced applications.

(2) Expansion in validation scope and application depth

Compared to Burggraaff et al. (2022), this study demonstrates a considerable expansion in both the breadth of validation and the depth of application. While Burggraaff et al. (2022) provided preliminary evidence for the accuracy of obtaining remote sensing radiance using calibrated smartphone RAW data, its validation was conducted on a limited scale. This study, however, undertakes a large-scale validation effort encompassing 267 sampling points across 15 distinct regions in China, which include water bodies with a wide range of optical characteristics from clear to highly turbid. This extensive validation robustly proves the method's powerful applicability and reliability across diverse aquatic environments.

(3) Progression from remote sensing reflectance correction to water quality monitoring

Furthermore, and most importantly, this study progresses beyond the stage of mere remote sensing reflectance correction. It advances into the practical domain of inverting a key water quality parameter (transparency) and conducts a comparative analysis between semi-empirical and semi-analytical models. This step provides a clear and evaluated pathway for the practical application of the method, moving from theoretical radiometric consistency to actionable environmental insights.

### 5.3 Applicability and uncertainty analysis

(1) Applicability of the method proposed in this study

From a technical perspective, the method proposed in this study is not limited to smartphones but can be extended to any digital camera capable of recording RAW-format images. Nevertheless, we focus on smartphones in this work because of their unique practical advantages, which are reflected in two aspects. First, smartphones enable convenient data transmission and cloud coordination. Thanks to their built-in communication modules, images captured by smartphones can be instantly uploaded to cloud platforms, supporting real-time processing and analysis using cloud-deployed water quality inversion algorithms. Second, smartphones integrate various auxiliary sensors, among which gyroscopes play a key role in ensuring accurate observation geometry. The inversion accuracy of water quality parameters often depends on stable viewing angles; The built-in gyroscope in a smartphone can record real-time posture information, helping users control or correct the shooting angle during data acquisition to meet the input requirements of the inversion model. This functionality is particularly important for non-expert users and in complex field environments.

(2) Uncertainty analysis of the method proposed in this study

It should be noted that the reflectance of reference cards varies across different brands and usage conditions, and this study has measured and verified such variability. However, requiring individual reflectance calibration for every reference

card used would hinder the large-scale deployment of crowdsourcing applications. Because the reference cards are gray, the resulting errors in remote sensing reflectance are generally similar across the RGB bands; therefore, subsequent water quality parameter inversion using band ratios or differences can reduce this uncertainty to some extent. Based on the above considerations, this study neglects the potential variation in the reflectance of the gray card during reference-card-based remote sensing reflectance correction.

The JPEG conversion algorithms employed by different camera manufacturers may vary and typically involve nonlinear image processing steps, which could introduce greater uncertainty than that associated with RAW format. Since this study focuses primarily on the water quality parameter inversion capability of RAW-format photos, JPEG format is not the main emphasis. Therefore, all subsequent analyses are based on RAW format data.

The errors reported in this study originate from two major sources: the errors introduced by the camera's imaging process and the uncertainties inherent in the inversion model. Consequently, the overall error should be considered the combined effect of both factors. Since this study did not quantitatively separate these two error components, it is difficult to precisely determine their individual contributions.

### 5.4 Implication for crowdsourced monitoring and future prospects

The findings of this study establish a solid technical foundation for utilizing smartphones in crowdsourced water quality monitoring. The simplified methodology (requiring only one reference card) coupled with guaranteed accuracy enables non-expert users to potentially contribute high-quality quantitative data. Looking ahead, the following research directions are particularly promising:

(1) Application development

The development of a smartphone application capable of automatically guiding users through the photo capture process (including angles, avoiding glint, etc.) and integrating the algorithms from this study would be transformative. Enabling "one-click" calculation of remote sensing reflectance and transparency would significantly promote the adoption of this method.

(2) Inversion of additional water quality parameters

While this study focused on transparency, future work should explore using the corrected remote sensing reflectance data to invert other critical water quality parameters, such as chlorophyll-*a* concentration, total suspended matter, and colored dissolved organic matter.

## 6 CONCLUSION

This study proposes a high-precision method for remote sensing reflectance correction and water quality parameter retrieval based on RAW-format smartphone photos, offering a practical tool for crowdsourced water quality monitoring. The findings demonstrate that water surface photos captured in RAW format can be used to accurately compute remote sensing reflectance, providing a robust foundation for high-precision retrieval of water quality parameters.

When the aperture and ISO are fixed while the shutter time is varied, the DN values of photos captured in RAW format exhibit a proportional relationship with exposure time for the same target. This enables normalization of DN values based on their linear relationship with exposure time, allowing different targets to be photographed under varying exposure conditions. Furthermore, the linear relationship between DN values and reflectance in RAW photos, with the regression line passing approximately through the origin, means that reflectance can be calculated using only a single gray card with known reflectance. This greatly facilitates the remote sensing reflectance correction process using RAW-format digital photographs.

This study processed RAW-format water surface images acquired from 267 sampling sites across 15 study areas. Remote sensing reflectance was derived using a gray card calibration method and validated against in situ equivalent remote sensing reflectance, demonstrating strong agreement with $R^2$ values ranging from 0.89 to 0.98. Based on the corrected reflectance, transparency retrieval was conducted using both semi-empirical and semi-analytical models. Comparative analysis revealed that the improved QAA-RGB-based semi-analytical model outperformed its semi-empirical counterpart, yielding higher accuracy with an $R^2$ of 0.78 and an RMSE of 0.6 m. These findings underscore the feasibility of using smartphone-acquired RAW imagery for reliable and feasible water quality inversion and provide a technical basis for advancing crowdsourced environmental monitoring applications.

## 7 DATA AVAILABILITY STATEMENT

The data that support the findings of this study are available from the corresponding author upon reasonable request.

**References**


Burggraaff O. 2020. Biases from incorrect reflectance convolution. *Optics Express*, **28**(9): 13801-13816, https://doi.org/10.1364/OE.391470.

Burggraaff O, Schmidt N, Zamorano J et al. 2019. Standardized spectral and radiometric calibration of consumer cameras. *Optics Express*, **27**(14): 19075-19101, https://doi.org/10.1364/OE.27.019075.

Burggraaff O, Werther M, Boss E S et al. 2022. Accuracy and reproducibility of above-water radiometry with calibrated smartphone cameras using RAW data. *Frontiers in Remote Sensing*, **3**: 940096, https://doi.org/10.3389/frsen.2022.940096.

Cao C, Li J S, Jia X D et al. 2024. Spatial and temporal variation of water clarity in typical reservoirs in the Beijing-Tianjin-Hebei region observed by GF1-WFV satellite data. *Journal of Oceanology and Limnology*, **42**(4): 1048-1060, https://doi.org/10.1007/s00343-024-3114-0.

Duan H T, Luo J H, Cao Z G et al. 2019. Progress in remote sensing of aquatic environments at the watershed scale. *Progress in Geography*, **38**(8): 1182-1195, https://doi.org/10.18306/dlkxjz.2019.08.007. (in Chinese)

Feng L, Wang X C. 2024. Quantifying cloud-free observations from Landsat missions: implications for water environment analysis. *Journal of Remote Sensing*, **4**: 0110, https://doi.org/10.34133/remotesensing.0110.

Gao M, Li J S, Wang S L et al. 2022. Smartphone-camera-based water reflectance measurement and typical water quality parameter inversion. *Remote Sensing*, **14**(6): 1371, https://doi.org/10.3390/rs14061371.

Gao M, Li J S, Zhang F F et al. 2020. Measurement of water leaving reflectance using a digital camera based on multiple reflectance reference cards. *Sensors*, **20**(22): 6580, https://doi.org/10.3390/s20226580.

He R Y, Lyu Z J, Jia S. 2024. Inversion of non-optical water quality parameters of hyperspectral remote sensing based on LBFGS-accelerated multi-layer perceptron network. *National Remote Sensing Bulletin*, **28**(11): 2970-2983, https://doi.org/10.11834/jrs.20243509. (in Chinese)

Hu M Q, Wang S L, Fang C et al. 2025. Remote sensing inversion of trophic states for typical lakes in China. *National Remote Sensing Bulletin*, **29**(11): 3296-3311, https://doi.org/10.11834/jrs.20254416. (in Chinese)

Huang X, Wang S Q, Yang D et al. 2024. Crowdsourcing geospatial data for earth and human observations: a review. *Journal of Remote Sensing*, **4**: 0105, https://doi.org/10.34133/remotesensing.0105.

IOCCG. 2006. Remote sensing of inherent optical properties: fundamentals, tests of algorithms, and applications. *In*: Lee Z P ed. Reports of the International Ocean-Colour Coordinating Group. IOCCG, Dartmouth. p.122.

Jiang X Z, Wang S L, Li J S et al. 2025. Water transparency and color in large rivers observed by Sentinel-2 MSI and its implications for SDG 6.3.2 monitoring. *International Journal of Applied Earth Observation and Geoinformation*, **143**: 104826, https://doi.org/10.1016/j.jag.2025.104826.

Lee Z P, Shang S L, Hu C M et al. 2015. Secchi disk depth: a new theory and mechanistic model for underwater visibility. *Remote Sensing of Environment*, **169**: 139-149, https://doi.org/10.1016/j.rse.2015.08.002.

Lee Z P, Shang S L, Lin G et al. 2016. On the modeling of hyperspectral remote-sensing reflectance of high-sediment-load waters in the visible to shortwave-infrared domain. *Applied Optics*, **55**(7): 1738-1750, https://doi.org/10.1364/AO.55.001738.

Leeuw T, Boss E. 2018. The HydroColor app: above water measurements of remote sensing reflectance and turbidity using a smartphone camera. *Sensors*, **18**(1): 256, https://doi.org/10.3390/s18010256.

Li J S, Gao M, Zhang B et al. 2022. Smartphone photo based water quality monitoring algorithm and application. *Acta Geodaetica et Cartographica Sinica*, **51**(4): 568-576, https://doi.org/10.11947/j.AGCS.2022.20220049. (in Chinese with English abstract)

Li J H, Xing Q G, Tian L Q et al. 2024. An improved UAV RGB image processing method for quantitative remote sensing of marine green macroalgae. *IEEE Journal of Selected Topics in Applied Earth Observations and Remote Sensing*, **17**: 19864-19883, https://doi.org/10.1109/JSTARS.2024.3486045.

Lukac R, Plataniotis K N. 2006. Single-sensor camera image compression. *IEEE Transactions on Consumer Electronics*, **52**(2): 299-307, https://doi.org/10.1109/TCE.2006.1649641.

Luo W, Li R, Shen F et al. 2023. HY-1C/D CZI image atmospheric correction and quantifying suspended particulate matter. *Remote Sensing*, **15**(2): 386, https://doi.org/10.3390/rs15020386.

Mahama P N J, Salama S M. 2024a. Calibration and validation of the HydroColor and Citclops smartphone applications for water quality monitoring. *Heliyon*, **10**(9): e30100, https://doi.org/10.1016/j.heliyon.2024.e30100.

Mahama P N J, Salama S M. 2024b. Innovative smartphone-based models for estimating water quality using RGB and XYZ colour spaces. *In*: Santiso ed. Scientific Research, New Technologies and Applications Vol. 1. p.1-35, https://doi.org/10.9734/bpi/srnta/v1/1999.

Malthus T J, Ohmsen R, Woerd H J v d. 2020. An evaluation of citizen science smartphone apps for inland water quality assessment. *Remote Sensing*, **12**(10): 1578, https://doi.org/10.3390/rs12101578.

Mueller J L, Fargion G S. 2002. Ocean optics protocols for satellite ocean color sensor validation. National Aeronautics and Space Administration, Goddard Space Flight Center, https://oceancolor.gsfc.nasa.gov/docs/technical/protocols.

Accessed on 2013-9-7.

Odermatt D, Danne O, Philipson P et al. 2018. Diversity II water quality parameters for 300 lakes worldwide from ENVISAT (2002-2012): a new global information source for lakes. *Earth System Science Data*, **10**(3): 1527-1549, https://doi.org/10.5194/essd-10-1527-2018.

Pitarch J, Vanhellemont Q. 2021. The QAA-RGB: a universal three-band absorption and backscattering retrieval algorithm for high resolution satellite sensors. Development and implementation in ACOLITE. *Remote Sensing Environment*, **265**: 112667, https://doi.org/10.1016/j.rse.2021.112667.

Prasad D K, Nguyen R, Brown M S. 2013. Quick approximation of camera's spectral response from casual lighting. *In*: 2013 IEEE International Conference on Computer Vision Workshops. IEEE, Sydney. p.844-851, https://doi.org/10.1109/ICCVW.2013.116.Accessed on 2014-3-6.

Ramezan C A, Warner T A, Maxwell A E. 2019. Evaluation of sampling and cross-validation tuning strategies for regional-scale machine learning classification. *Remote Sensing*, **11**(2): 185, https://doi.org/10.3390/rs11020185.

Song X Y, Li J S, Zhang F F et al. 2025. Assessing four-decade spatiotemporal changes of chlorophyll-*a* concentration in lakes and reservoirs of the mid-Lower Yangtze River Basin using Landsat imagery and machine learning. *International Journal of Applied Earth Observations and Geoinformation*, **144**: 104957, https://doi.org/10.1016/j.jag.2025.104957.

Wang S L, Jiang X J, Spyrakos E et al. 2024. Water color from Sentinel-2 MSI data for monitoring large rivers: Yangtze and Danube. *Geo-Spatial Information Science*, **27**(3): 854-869, https://doi.org/10.1080/10095020.2023.2258950.

Wang S L, Li J S, Zhang B et al. 2018. Trophic state assessment of global inland waters using a MODIS-derived Forel-Ule index. *Remote Sensing Environment*, **217**: 444-460, https://doi.org/10.1016/j.rse.2018.08.026.

Wang S L, Li J S, Zhang B et al. 2020. Changes of water clarity in large lakes and reservoirs across China observed from long-term MODIS. *Remote Sensing Environment*, **247**: 111949, https://doi.org/10.1016/j.rse.2020.111949.

Yin Z Y, Li J S, Huang J et al. 2021a. Steady increase in water clarity in Jiaozhou Bay in the Yellow Sea from 2000 to 2018: observations from MODIS. *Journal of Oceanology and Limnology*, **39**(3): 800-813, https://doi.org/10.1007/s00343-020-0124-4.

Yin Z Y, Li J S, Liu Y et al. 2021b. Water clarity changes in Lake Taihu over 36 years based on Landsat TM and OLI observations. *International Journal of Applied Earth Observation and Geoinformation*, **102**: 102457, https://doi.org/10.1016/j.jag.2021.102457.

Yin Z Y, Li J S, Zhang B et al. 2023. Increase in chlorophyll-*a* concentration in Lake Taihu from 1984 to 2021 based on Landsat observations. *Science of the Total Environment*, **873**: 162168, https://doi.org/10.1016/j.scitotenv.2023.162168.

Zeng F X, Song C Q, Cao Z G et al. 2023. Monitoring inland water via Sentinel satellite constellation: a review and perspective. *ISPRS Journal of Photogrammetry and Remote Sensing*, **204**: 340-361, https://doi.org/10.1016/j.isprsjprs.2023.09.011.

Zhang B, Li J S, Shen Q et al. 2021a. Recent research progress on long time series and large scale optical remote sensing of inland water. *National Remote Sensing Bulletin*, **25**(1): 37-52, https://doi.org/10.11834/jrs.20210570. (in Chinese)

Zhang Y L, Shi K, Zhang Y B et al. 2021b. The proposal, practice and preliminary application of land-based (ground-based, shore-based) remote sensing of water environment. *National Remote Sensing Bulletin*, **25**(11): 2163-2172, https://doi.org/10.11834/jrs.20210473.

## Electronic supplementary material

Supplementary material (Supplementary Tables S1–S4 and Figs.S1–S4) is available in the online version of this article at https://doi.org/10.1007/s00343-026-6004-9.